Review of Scientific Instruments

High energy x-ray diffraction/x-ray fluorescence spectroscopy for high-throughput analysis of composition spread thin films

Cite as: Rev. Sci. Instrum. **80**, 123905 (2009); https://doi.org/10.1063/1.3274179
Submitted: 19 October 2009 . Accepted: 22 November 2009 . Published Online: 28 December 2009

John M. Gregoire, Darren Dale, Alexander Kazimirov, Francis J. DiSalvo, and R. Bruce van Dover

View Online Export Citation

ARTICLES YOU MAY BE INTERESTED IN

Applications of high throughput (combinatorial) methodologies to electronic, magnetic, optical, and energy-related materials
Journal of Applied Physics **113**, 231101 (2013); https://doi.org/10.1063/1.4803530

A wavelet transform algorithm for peak detection and application to powder x-ray diffraction data
Review of Scientific Instruments **82**, 015105 (2011); https://doi.org/10.1063/1.3505103

Fulfilling the promise of the materials genome initiative with high-throughput experimental methodologies
Applied Physics Reviews **4**, 011105 (2017); https://doi.org/10.1063/1.4977487

MCL MAD CITY LABS INC. www.madcitylabs.com
Nanopositioning Systems
Modular Motion Control
AFM and NSOM Instruments
Single Molecule Microscopes



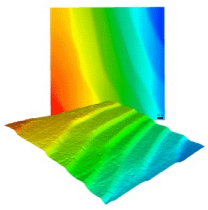
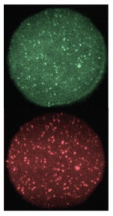

© 2009 American Institute of Physics.

AIP Publishing

High energy x-ray diffraction/x-ray fluorescence spectroscopy for high-throughput analysis of composition spread thin films

John M. Gregoire,[1] Darren Dale,[2] Alexander Kazimirov,[2] Francis J. DiSalvo,[3] and R. Bruce van Dover[4]
[1]*Department of Physics, and Cornell Fuel Cell Institute, Cornell University, Ithaca, New York 14853, USA*
[2]*Cornell High Energy Synchrotron Source, Cornell University, New York 14853, USA*
[3]*Department of Chemistry and Chemical Biology, and Cornell Fuel Cell Institute, Cornell University, New York 14853, USA*
[4]*Department of Materials Science and Engineering, and Cornell Fuel Cell Institute, Cornell University, New York 14853, USA*

(Received 19 October 2009; accepted 22 November 2009; published online 28 December 2009)

High-throughput crystallography is an important tool in materials research, particularly for the rapid assessment of structure-property relationships. We present a technique for simultaneous acquisition of diffraction images and fluorescence spectra on a continuous composition spread thin film using a 60 keV x-ray source. Subsequent noninteractive data processing provides maps of the diffraction profiles, thin film fiber texture, and composition. Even for highly textured films, our diffraction technique provides detection of diffraction from each family of Bragg reflections, which affords direct comparison of the measured profiles with powder patterns of known phases. These techniques are important for high throughput combinatorial studies as they provide structure and composition maps which may be correlated with performance trends within an inorganic library.
© *2009 American Institute of Physics.* [doi:10.1063/1.3274179]

I. INTRODUCTION

Analysis of inorganic libraries is an increasingly useful technique for materials discovery and optimization, as evident in the number and variety of recently published methods for combinatorial materials research.[1–3] We have recently presented methods for high throughput screening of continuous composition spread thin films for fuel cell oxidation catalysis.[4,5] In this research, binary or ternary continuous composition spreads are sputter deposited onto Si substrates from elemental metal targets. The entire composition spread is then evaluated as a catalyst (e.g., for the oxidation of methanol) and the catalytically active regions are determined. We anticipate that the three aspects of bulk structure that will best correlate with trends in catalytic activity are film composition, crystalline phase, and fiber texture. The goal is thus to measure these as a function of substrate position and correlate the results with the independent measurements of catalytic activity. This type of analysis is at the frontier of combinatorial materials research. For example, principle component analysis has recently been applied to the problem of heterogeneous catalysis using only composition variables as components.[6] The ability to include crystalline phase and fiber texture in this type of analysis would greatly facilitate the discovery of new materials not only for catalysis but also for the broad range of applications conducive to investigation with combinatorial methods. We present a simple configuration for simultaneous measurement of thin film composition, thickness, structure, and fiber texture using high-energy x-ray diffraction (XRD) and energy-dispersive x-ray fluorescence spectroscopy (XRF).

Synchrotron radiation has previously been employed for mapping the composition[7] and structure[8] of inorganic libraries, and these techniques have recently been combined in a single experiment.[9] XRD analysis of fiber textured thin films typically involves the mapping of diffraction over both the fiber texture angle and scattering angle. Multiaxial scans may be used to sweep through these angles[10] but such experiments are generally time intensive. Several techniques for fiber texture analysis have been developed with high energy XRD and area detectors.[11] Recently, Kukuruznyak *et al.*[12] have adopted this type of experiment for the analysis of ternary oxide composition spreads. In their study, the diffraction data acquired at many positions in the composition spread were used to determine not only the phase behavior but also the regions exhibiting an epitaxial relation to the underlying substrate. We present data processing techniques which afford simplifications compared to these diffraction experiments and are optimized for analysis of fiber-textured thin films.

Batch analysis of the large data sets acquired during characterization of composition libraries is an active area of research. Barr and co-workers[13,14] demonstrated significant advancements in the analysis of powder XRD patterns from organic libraries using principal-component analysis, metric multidimensional scaling, and clustering techniques. These techniques have been adapted for the analysis of inorganic libraries[15] but several properties of inorganic libraries pose significant problems for these algorithms. One particular challenge is the automated detection of phases in multiphase samples. For comparison of the diffraction profile of an unknown phase with indexed diffraction patterns, it is important to detect at least one Bragg reflection from each Miller index family with finite scattering intensity. In the analysis of

 © 2009 American Institute of Physics

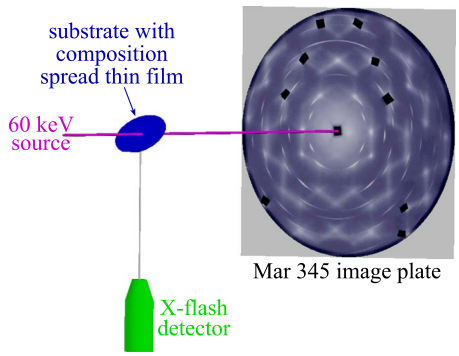

FIG. 1. (Color online) Schematic of the XRD/XRF equipment in the CHESS A2 hutch. The schematic is approximately to scale, and the Mar 345 image shown in the outline of the detector is a typical diffraction image acquired on a composition spread thin film.

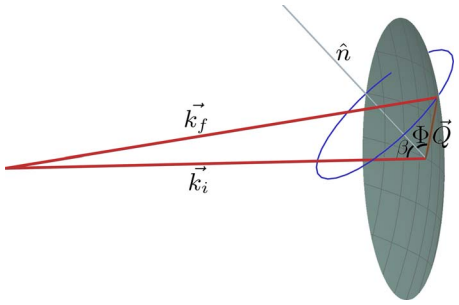

FIG. 2. (Color online) The reciprocal space geometry for the diffraction experiment is shown with the substrate normal $\hat{n}$ displaced β=46° from the initial wave vector $\vec{k}_i$. The green spherical section denotes the section of the Ewald sphere intersected by the image plate detector. A scattering vector $\vec{Q}$ which intercepts the Ewald sphere is shown along with the corresponding final wave vector $\vec{k}_f$. The fiber texture ring formed by procession of $\vec{Q}$ about $\hat{n}$ is shown in blue. For the reciprocal lattice vector at $\vec{Q}$, the angular displacement from $\hat{n}$, i.e., the fiber texture angle Φ, is also indicated.

fiber textured samples, many traditional diffraction experiments do not meet this requirement due to inadequate sampling of reciprocal space, and phase identification is often confounded by the absence of peaks in the measured diffraction patterns. This issue is addressed in the present work by adopting a diffraction geometry that provides detection over a wide range of fiber texture angles. Also, our use of high x-ray energy affords detection of high order Bragg reflections, facilitating phase identification.

II. EXPERIMENTAL

A. Thin film deposition

Thin film composition spreads are prepared by magnetron cosputtering in a deposition system that has been described previously.[16] The composition spread discussed in this manuscript was prepared using a prime grade Si substrate (76.2 mm diameter, 350 μm thick, (100) orientation, single-side polished). A uniform 7nm Ti adhesion and heating layer was deposited on the substrate, followed by codeposition of Pt and Ru in an atmosphere of 0.67 Pa Ar. Using a quartz crystal monitor, the Pt and Ru rates were independently measured to be 2×10^{-9} mol/s/cm^2 at substrate center. The independent Pt and Ru dc power sources were operated at 129 mA, 353 V, and 162 mA, 355 V, respectively, and the substrate was maintained at 400 °C during the 420 s deposition.

The XRD/XRF experiments were performed at the A2 line of the Cornell High Energy Synchrotron Source (CHESS). A schematic of the experimental layout is given in Fig. 1. The diffraction images were measured in transmission geometry with a Mar 345 image plate detector oriented normal to the incident beam. A x-flash detector was displaced by 90° from the incident beam, and the substrate was oriented such that the thin film faces the Mar 345 and x-flash detectors.

The sample to Mar 345 distance was 0.55 m and calibrated using a Si powder mounted at the film position. In this geometry, the 60 keV x-ray energy provides detection of Bragg reflections with d spacings ranging from 0.05 to 0.5 nm, the primary range of interest for inorganic materials.

A goniometer provides β=46° substrate tilt with respect to the incident beam, and a translation stage mounted to the goniometer provides positioning of the composition spread thin film with respect to the incident beam. Data acquisition is performed by defining a rectangular grid of substrate positions and employing an automated data acquisition system which acquires diffraction images and fluorescence spectra at the subset of positions within the bounds of the composition spread. The collimated incident beam has a 1.2 mm square footprint on the tilted substrate, and thus each measurement is an average over a ~1 at. % composition range of the composition spread thin film.[16]

A 1.6-mm-thick Al plate is mounted on the front of the Mar 345 detector and serves as a passive high-pass x-ray energy filter, which is used to improve signal-to-noise in the diffraction image by attenuating XRF that is emitted isotropically by the sample. As discussed in Sec. III B, the diffraction images contain thermal diffuse scattering from the Si substrate, which in several detector regions is orders of magnitude more intense than the thin film reflections. To avoid saturation of the image plate in these positions, small Pb beam stops were taped onto the Al plate. The substrate holder is machined to provide nearly identical mounting of each substrate. As a result, data acquisition for each composition spread results in a fairly constant Si thermal diffuse scattering profile so that the Pb pieces do not need to be moved. The substrate is secured with polyimide tape to avoid stress-induced curvature in the Si substrate, which would result in substantial variation in the thermal diffuse scattering profile as a function of substrate position.

The substrate is not rotated during acquisition, precluding the study of single crystalline films. The films are assumed to be either equiaxed or fiber textured, a common property of metal thin films deposited onto a polycrystalline underlayer. The reciprocal space geometry of the experimental configuration is presented in Fig. 2 for the case of fiber texture along substrate normal. For a given (hkl) of a single-phase fiber textured thin film, the set of reciprocal lattice vectors from the crystalline grains have an isotropic azimuthal distribution. The ensemble of these (hkl) vectors thus lie on a circle in reciprocal space. The azimuthal angle, typically denoted ϕ, is not labeled in Fig. 2, but an example fiber texture ring is drawn. Note that if the substrate normal $\hat{n}$

were coaxial with the incident wave vector $\vec{k}_i$, the depicted texture ring would not intersect the Ewald sphere.

Fiber texture is analyzed as a function of the angular displacement Φ of the scattering vector with respect to substrate normal. In the presented geometry, the range of Φ is determined by the angle β between the substrate normal and the incident beam with $\pi/2-\theta-\beta<\Phi<\pi/2-\theta+\beta$ for a given scattering angle 2θ. For a fiber textured film of a given phase, the goal is to detect at least one reflection from each distinct family of Miller indices {hkl} which give rise to appreciable diffraction intensity. The necessary range of Φ detection depends on the crystal symmetry and fiber texture direction. For the case of cubic symmetry, any continuous Φ range in excess of $\pi/2$ is sufficient. For analysis of fiber textured films with a different crystal symmetry, the tilt angle β should be chosen such that the angle Φ between the surface normal and the diffraction ring of interest is within the above range. The $\beta=46°$ tilt in the presented geometry results in a Φ detection range of 92° for each scattering angle and thus provides detection of a sufficient number of {hkl} families for phase identification. We note that due to the detection of a subset of the reflections in the family {hkl}, the relative peak intensities of powder patterns derived from the diffraction images may differ from those of indexed powder diffraction patterns.

III. DATA PROCESSING, RESULTS, AND DISCUSSION

As discussed above, noninteractive analysis of characterization data is an active field of research in combinatorial material science. For processing the XRD/XRF data, we have combined established algorithms with new analysis techniques into a software platform written in the PYTHON programming language.

A. XRF-determined composition and thickness

We previously presented algorithms for calculating cosputtered film composition from measured deposition profiles.[17,18] For the Pt–Ru composition spread, the estimated accuracy of the calculated composition x in Pt_xRu_{1-x} is 5 at. % or less. The well-established deposition profiles provide even better relative composition accuracy and serve as a standard for verification of the XRF-determined composition.

The analysis of the set of XRF spectra from a given composition spread is performed with a noninteractive procedure which employs routines from the PYMCA software package.[19] Each spectrum is independently processed for elemental peak identification and profile fitting. The absolute and relative intensities of the characteristic peaks of the elements of interest (e.g., Pt–L and Ru–K) are then used in an iterative procedure which simultaneously solves for a self-consistent estimation of the absolute mass and relative mass fraction. While composition estimates can be used to seed the iterative routine, we found that the same results were obtained regardless of seed value. Additionally, the routine converged within $\lesssim$10 iterations for each spectrum.

An example fitted XRF spectrum is shown in Fig. 3. The figure demonstrates proper fitting of the fluorescence from

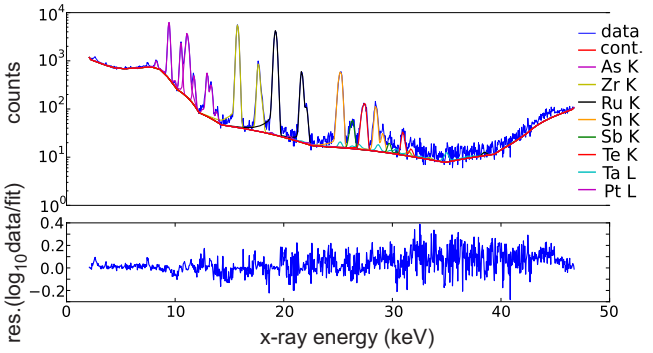

FIG. 3. (Color online) The XRF spectrum from the center position of the Pt–Ru film. The components of the fit spectrum, including the continuum background "cont.," are plotted with the raw data (top). The logarithmic residual spectrum (bottom) demonstrates that all data peaks have been identified and properly fit. In addition to the film elements and As dopants in the substrate, the spectrum includes fluorescence from trace Ta impurities in the underlayer and four elements from unintentional detection of a different fluorescence source.

the thin film as well as artifacts attributed to the fluorescence of other materials in the apparatus. The artifacts have a negligible impact on the calculation of Pt and Ru composition and will be eliminated in future experiments by additional shielding.

For the Pt–Ru composition spread, the compositions and thicknesses calculated using this algorithm are plotted in Figs. 4(a) and 5. The smoothness of the interpolated contours in these plots is indicative of the negligible uncertainties in the calculated intensities of the fluorescence peaks. Each XRF-calculated composition differs by less than 3 at. % from the respective deposition profile calculation [Fig. 4(b)]. The discrepancies are well within the uncertainties of the deposition profiles, and the agreement demonstrates the validity of the XRF data processing algorithms. For the Pt–Ru system we estimate a 3 at. % uncertainty in the calculated composition and note that this uncertainty is strongly dependent on the chemical system.

The thickness determination is highly dependent on the x-ray dose. While this quantity may be determined through analysis of a standard calibrant to provide absolute thickness measurements of the thin films, we performed a calibration using the XRF spectrum from substrate center and the crystal monitor-determined film thickness at this position. Given the x-ray dose, which is kept constant for all analyzed substrate positions, each thickness value is calculated using the film density and absolute mass determined by the iterative procedure described above.

The calculation of the film thickness from the XRF-determined column density requires an estimate of the film density. In the generation of the thickness map of Fig. 5, we estimated the cosputtered film density to be the weighted average of bulk Pt and Ru densities. Since our characterization technique also provides a phase map of the thin film composition spread, the film density could be more accurately determined by using the weighted average of the molar volumes for each crystallographic phase.

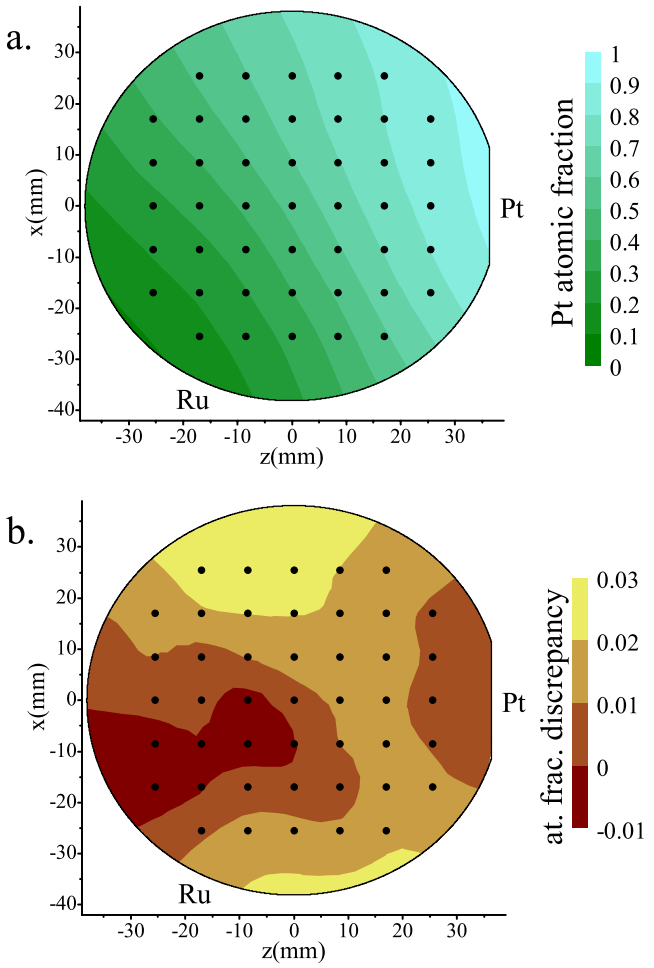

FIG. 4. (Color online) Interpolated contour plots show the XRF-determined profile of the atomic fraction Pt (a) and its deviation from that of the deposition profile calculations (b) for the Pt–Ru composition spread thin film. The plots are within an outline of the Si substrate and the element symbols denote the orientation of the respective deposition source with respect to the substrate. The black points show the substrate positions used in high energy XRD/XRF data acquisition.

B. XRD image processing and diffraction profile analysis

As described above, the diffraction images contain thermal diffuse scattering from the Si substrate which should be removed during data processing to facilitate comparison of the diffraction data to indexed powder patterns. Similarly, the diffraction images contain unwanted intensity due to x-ray scattering with air and the underlayer film, although the underlayer is weakly scattering in the Pt–Ru sample discussed in this manuscript. Kukuruznyak *et al.*[12] perform background subtraction via measured diffraction images which are acquired at substrate regions without deposited material. For composition spread thin film deposition, the inclusion of such a region in each composition spread requires either a deposition mask or postdeposition film removal. Our common use of elevated substrate temperature during deposition inhibits deposition masking, and both techniques would impede upon the high-throughput nature of the research. Instead, we introduce an algorithm by which a background subtraction image is calculated from the set of diffraction images acquired on a single composition spread.

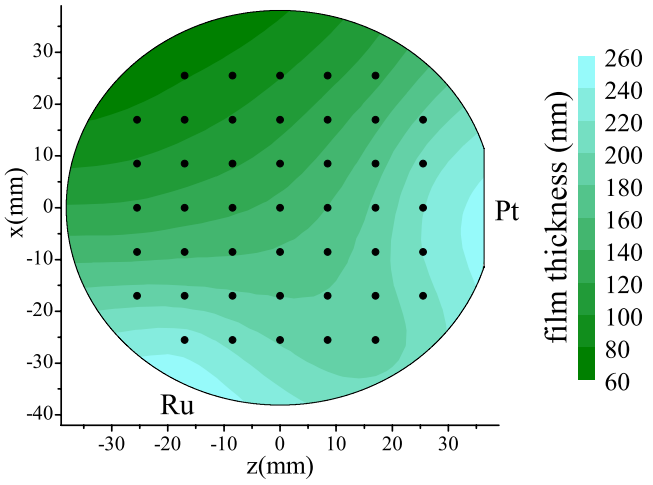

FIG. 5. (Color online) The interpolated contour plot shows the XRF-determined profile of the Pt–Ru film thickness. The plots are within an outline of the Si substrate and the element symbols denote the orientation of the respective deposition source with respect to the substrate. The black points show the substrate positions used in high energy XRD/XRF data acquisition.

Since each diffraction is acquired using a predetermined (incoherent) x-ray dose, scatterers that are common to every sample analyzed in a data set (the set of points in Figs. 4 and 5) will provide the same diffraction intensity in every image. The intensity of a given pixel in the calculated background image is the minimum intensity obtained by that pixel in the set of all diffraction images acquired on the composition spread. This algorithm assumes that for every detector pixel, there will be at least one diffraction image in the data set that contains no diffraction intensity from the composition spread thin film. This assumption is commonly met in composition spread thin films due to lattice constant shifts and phase changes as a function of film composition. That is, we exploit the fact that by sampling the thin film over a wide range of compositions, we ensure that any Bragg reflections from the thin film are not in every diffraction image. The implementation of this simple algorithm includes the exclusion of low-intensity outliers in the intensity distribution of each pixel and smoothing of the background image. Also, the calculated background image is inspected for inclusion of film Bragg reflections which may exist in the event that the above assumptions are not realized. In this case, the intensity in these regions of the background image is calculated by interpolation of the surrounding data. While this background-correction routine is not automated, it requires user analysis of only one diffraction image per composition spread.

For the substrate center point in the Pt–Ru composition spread, Fig. 6 shows the raw diffraction image, the calculated background image and the difference image that is used in subsequent analysis. The incomplete arcs in Fig. 6(c) indicate that the film is fiber textured. Azimuthal integration of this image (with appropriate $d|\vec{Q}|d\Phi$ weighting) yields the analog of a powder pattern which is then processed to the final spectrum used for phase identification [Fig. 7(b)]. Although not depicted in Fig. 6, we note that the detector regions immediately surrounding the Pb blocks are excluded

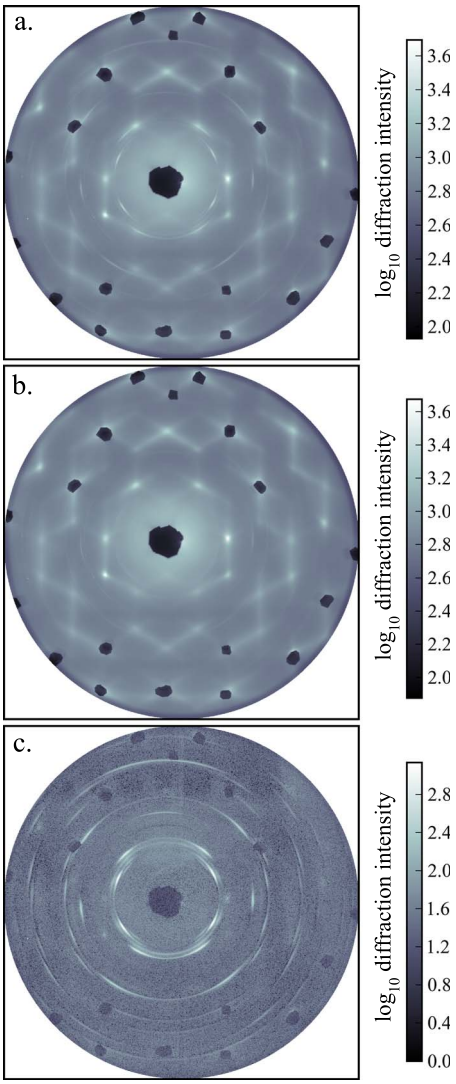

FIG. 6. (Color online) The background subtraction for the diffraction image acquired at substrate center is illustrated. The raw diffraction image (a) is plotted with the background image (b) that is common to the entire data set. The difference image (c) shows the presence of many Pt and Ru Bragg reflections and demonstrates the effectiveness of the background subtraction.

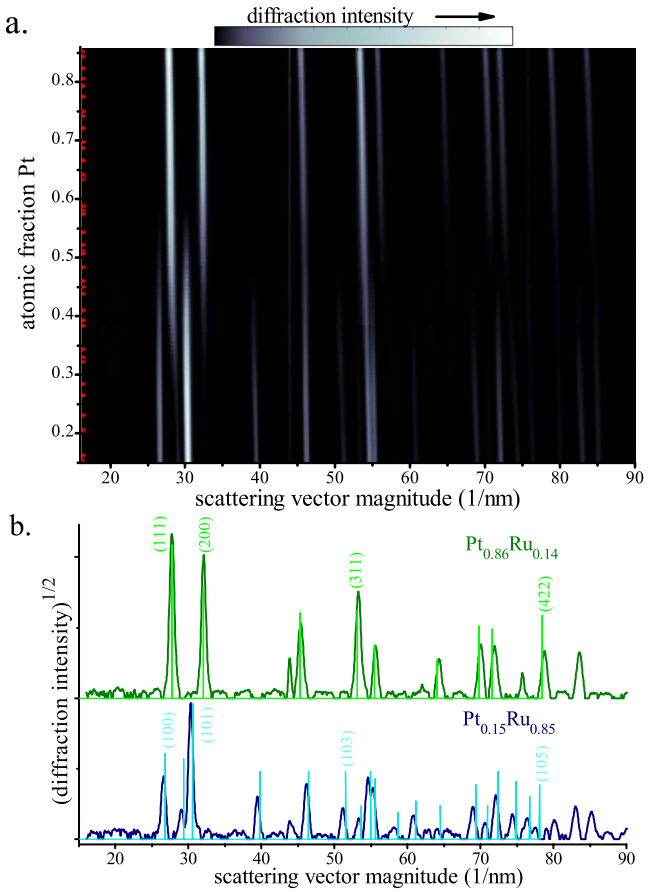

FIG. 7. (Color online) (a) The diffraction profiles from the 45 measurements on the Pt–Ru composition spread are plotted with interpolation along the composition (vertical) axis. The XRF-determined compositions of the measured samples are noted by red markers along the vertical axis. Each profile is normalized by the respective XRF-determined thin film mass. The alloying of the two elements is evident in the slope of the diffraction peaks as a function of composition, and the two-phase region is easily identified. (b) The profiles of the most Pt-rich and Ru-rich samples are plotted along with the indexed powder patterns for fcc Pt (top) and hcp-Ru (bottom) (Ref. 22). The peak shifting due to alloying is evident, and the profiles show high-order peaks in the high scattering vector range which are not included in the indexed patterns.

from analysis. Inspection of the map of the diffraction patterns as a function of composition [Fig. 7(a)] yields rapid determination of the qualitative phase behavior in the film. In the Pt–Ru film, two single-phase regions and the combined two-phase region are identified, in agreement with the bulk equilibrium phase diagram.

C. Fiber texture analysis

The fiber texture of the film is determined by analysis of the Φ distributions of identified Bragg reflections in the diffraction profiles. Figure 8 demonstrates the identification of Pt(111) and Ru(001) fiber texture in the composition spread thin film. The peaks in the Φ distribution deviate from the values calculated under the assumption that the fiber texture direction is substrate normal. Such deviations commonly arise in sputter deposited thin films due to anisotropic residual stress or alterations in the film growth direction arising from oblique deposition.[20] While these phenomena may be investigated through calculation of the orientation distribution function from the Φ distributions of the detected Bragg reflections,[21] such analysis is beyond the scope of this manuscript. We note that Fig. 8 is indicative of a fiber texture direction that is tilted by ~6° toward the Pt deposition source.

IV. CONCLUSIONS

We present a high-energy XRD/XRF experiment for analysis of composition spread thin films. We also present data processing algorithms that provide mapping of the film composition, thickness, diffraction profiles, and fiber texture as a function of position in the composition spread. The phase behavior of the chemical system is determined through combined analysis of the composition mapping and diffraction patterns. Thus, the primary bulk properties of the composition spread are determined in a single experiment.

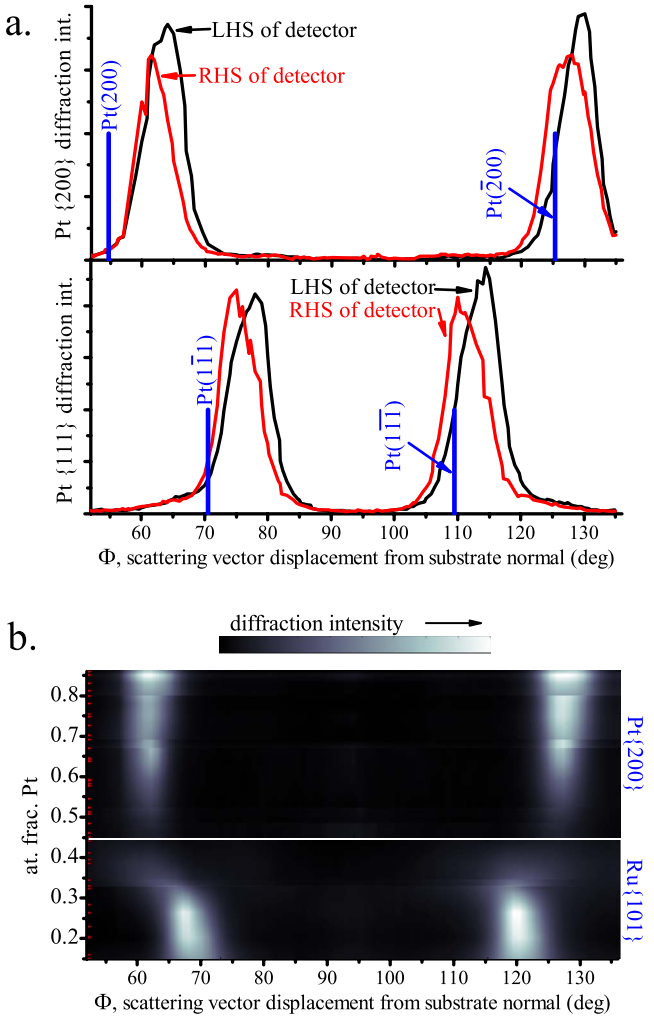

FIG. 8. (Color online) The diffraction intensity profiles of the Pt{200} (a) and Pt{111} (b) Bragg reflections are plotted as a function of the scattering vector angular displacement Φ from substrate normal. Analysis of these distributions reveals that the film is fiber textured about Pt(111). Different distributions are plotted for left-hand side (LHS) and right-hand side (RHS) of the detector, which correspond to the sampling of reciprocal space on different sides of the plane defined by $\vec{k}_i$ and $\hat{n}$ (see Fig. 2). (c) Using only the RHS of the 45 diffraction images, the Φ distributions of the Pt{200} and Ru{101} are plotted as a function of the atomic fraction of Pt. The Pt{200} (Ru{101}) distribution is shown over the composition range where the fcc-Pt (hcp-Ru) phase is dominant. Following the fiber texture analysis of (a) and (b), the plot indicates that the fcc-Pt alloys maintain Pt(111) fiber texture over the entire composition range. Similarly, the plot demonstrates that the hcp-Ru alloys maintain Ru(001) fiber texture.

This important advancement in high throughput characterization provides rapid assessment of property maps which can be compared with independently determined performance data to reveal important trends.

ACKNOWLEDGMENTS

This work is based upon research conducted at the Cornell High Energy Synchrotron Source (CHESS) which is supported by the National Science Foundation and the National Institutes of Health/National Institute of General Medical Sciences under NSF award DMR-0225180. This work was also supported by the Cornell Fuel Cell Institute funded by the Department of Energy (Grant No. ER06-02-13022-11751-11792). The authors thank Michele Tague, Anna Legard, and Taro Naoi for assistance in data acquisition.

[1] Z. H. Barber and M. G. Blamire, Mater. Sci. Technol. **24**, 757 (2008).
[2] *Combinatorial and High-Throughput Discovery and Optimization of Catalysts and Materials*, edited by R. A. Potyrailo and W. F. Maier (CRC, Boca Raton, 2007).
[3] R. van Dover and L. Schneemeyer, Macromol. Rapid Commun. **25**, 150 (2004).
[4] M. Prochaska, J. Jin, D. Rochefort, L. Zhuang, F. DiSalvo, H. Abruña, and R. van Dover, Rev. Sci. Instrum. **77**, 054104 (2006).
[5] J. M. Gregoire, M. Kostylev, M. E. Tague, P. F. Mutolo, R. B. van Dover, F. J. DiSalvo, and H. D. Abruña, J. Electrochem. Soc. **156**, B160 (2009).
[6] S. C. Sieg, C. Suh, T. Schmidt, M. Stukowski, K. Rajan, and W. F. Maier, QSAR Comb. Sci. **26**, 528 (2007).
[7] S. Vogt, Y. Chu, A. Tkachuk, P. Ilinski, D. Walko, and F. Tsui, Appl. Surf. Sci. **223**, 214 (2004).
[8] Y. Chu, A. Tkachuk, S. Vogt, P. Ilinski, D. Walko, D. Mancini, E. Dufresne, L. He, and F. Tsui, Appl. Surf. Sci. **223**, 175 (2004).
[9] B. Xia, Y. S. Chu, and W. L. Gladfelter, Surf. Coat. Technol. **201**, 9041 (2007).
[10] C. Borgia, S. Olliges, and R. Spolenak, Rev. Sci. Instrum. **79**, 043904 (2008).
[11] K. Kawasaki and H. Iwasaki, J. Synchrotron Radiat. **2**, 49 (1995).
[12] D. A. Kukuruznyak, H. Reichert, J. Okasinski, H. Dosch, T. Chikyow, J. Daniels, and V. Honkimaeki, Appl. Phys. Lett. **91**, 071916 (2007).
[13] G. Barr, W. Dong, and C. Gilmore, J. Appl. Crystallogr. **37**, 658 (2004).
[14] G. Barr, W. Dong, C. Gilmore, A. Parkin, and C. Wilson, J. Appl. Crystallogr. **38**, 833 (2005).
[15] C. J. Long, J. Hattrick-Simpers, M. Murakami, R. C. Srivastava, I. Takeuchi, V. L. Karen, and X. Li, Rev. Sci. Instrum. **78**, 072217 (2007).
[16] J. M. Gregoire, R. B. van Dover, J. Jin, F. J. DiSalvo, and H. D. Abruña, Rev. Sci. Instrum. **78**, 072212 (2007).
[17] J. M. Gregoire, M. B. Lobovsky, M. F. Heinz, F. J. DiSalvo, and R. B. van Dover, Phys. Rev. B **76**, 195437 (2007).
[18] J. M. Gregoire and R. B. van Dover, J. Vac. Sci. Technol. A **26**, 1030 (2008).
[19] V. Solé, E. Papillon, M. Cotte, P. Walter, and J. Susini, Spectrochim. Acta, Part A **B62**, 63 (2007).
[20] M. Ohring, *Materials Science of Thin Films*, 2nd ed. (Academic, New York, 2002).
[21] M. Kocks, C. N. Tomé, and H. R. Wenk, *Texture and Anisotropy* (Cambridge University Press, Cambridge, 1998).
[22] JCPDS Card Nos. 040802 and 060663.